Growth and characterization of SiGeSn quantum well photodiodes

Inga A. Fischer,[1,*] Torsten Wendav,[2] Lion Augel,[1] Songchai Jitpakdeebodin,[1] Filipe Oliveira,[1] Alessandro Benedetti,[3] Stefan Stefanov,[4] Stefano Chiussi,[4] Giovanni Capellini,[5] Kurt Busch,[2,6] and Jörg Schulze[1]

[1]Institut für Halbleitertechnik (IHT), Universität Stuttgart, Pfaffenwaldring 47, Stuttgart, 70569, Germany
[2]Humboldt-Universität zu Berlin, Institut für Physik, AG Theoretische Optik & Photonik, Germany
[3]CACTI, Univ. de Vigo, Campus Universitario Lagoas Marcosende 15, Vigo, Spain
[4]Dpto. Física Aplicada, Univ. de Vigo, Rua Maxwell s/n, Campus Universitario Lagoas Marcosende, Vigo, Spain
[5]IHP, Im Technologiepark 25, 15236 Frankfurt (Oder), Germany
[6]Max-Born-Institut, 12489 Berlin, Germany
[*]fischer@iht.uni-stuttgart.de

Abstract: We report on the fabrication and electro-optical characterization of SiGeSn multi-quantum well PIN diodes. Two types of PIN diodes, in which two and four quantum wells with well and barrier thicknesses of 10 nm each are sandwiched between B- and Sb-doped Ge-regions, were fabricated as single-mesa devices, using a low-temperature fabrication process. We discuss measurements of the diode characteristics, optical responsivity and room-temperature electroluminescence and compare with theoretical predictions from band structure calculations.

OCIS codes: (250.5590) Quantum-well, -wire and -dot devices; (230.5160) Photodetectors; (230.3670) Light-emitting diodes.

References and links

1. L. Jiang, J. D. Gallagher, C. L. Senaratne, T. Aoki, J. Mathews, J. Kouvetakis, and J. Menéndez, "Compositional dependence of the direct and indirect band gaps in $Ge_{1-y}Sn_y$ alloys from room temperature photoluminescence: implications for the indirect to direct gap crossover in intrinsic and n-type materials," Semicond. Sci. Technol. **29**(11), 115028 (2014).
2. A. A. Tonkikh, C. Eisenschmidt, V. G. Talalaev, N. D. Zakharov, J. Schilling, G. Schmidt, and P. Werner, "Pseudomorphic GeSn/Ge(001) quantum wells: examining indirect band gap bowing," Appl. Phys. Lett. **103**(3), 032106 (2013).
3. J. Mathews, R. Roucka, J. Xie, S.-Q. Yu, J. Menéndez, and J. Kouvetakis, "Extended performance GeSn/Si(100) p-i-n photodetectors for full spectral range telecommunication applications," Appl. Phys. Lett. **95**(13), 133506 (2009).
4. R. Roucka, J. Mathews, C. Weng, R. T. Beeler, J. Tolle, J. Menéndez, and J. Kouvetakis, "High-performance near-IR photodiodes: a novel chemistry-based approach to Ge and Ge-Sn devices integrated on Silicon," IEEE J. Quantum Electron. **47**(2), 213–222 (2011).
5. J. Werner, M. Oehme, M. Schmid, M. Kaschel, A. Schirmer, E. Kasper, and J. Schulze, "Germanium-Tin p-i-n photodetectors integrated on Silicon grown by molecular beam epitaxy," Appl. Phys. Lett. **98**(6), 061108 (2011).
6. D. L. Zhang, C. L. Xue, B. W. Cheng, S. J. Su, Z. Liu, X. Zhang, G. Z. Zhang, C. B. Li, and Q. M. Wang, "High-responsivity GeSn short-wave infrared p-i-n photodetectors," Appl. Phys. Lett. **102**(14), 141111 (2013).
7. M. Oehme, D. Widmann, K. Kostecki, P. Zaumseil, B. Schwartz, M. Gollhofer, R. Koerner, S. Bechler, M. Kittler, E. Kasper, and J. Schulze, "GeSn/Ge multiquantum well photodetectors on Si substrates," Opt. Lett. **39**(16), 4711–4714 (2014).
8. V. R. D'Costa, Y.-Y. Fang, J. Tolle, J. Kouvetakis, and J. Menéndez, "Tunable optical gap at a fixed lattice constant in group-IV semiconductor alloys," Phys. Rev. Lett. **102**(10), 107403 (2009).
9. R. A. Soref, J. Kouvetakis, and J. Menendez, "Advances in SiGeSn/Ge technology," Mater. Res. Soc. Symp. Proc., **958**, 0958L (2007).
10. L. Jiang, C. Xu, J. D. Gallagher, R. Favaro, T. Aoki, J. Menéndez, and J. Kouvetakis, "Development of light emitting group IV ternary alloys on Si platforms for long wavelength optoelectronic applications," Chem. Mater. **26**(8), 2522–2531 (2014).
11. S. Wirths, D. Buca, Z. Ikonic, P. Harrison, A. T. Tiedemann, B. Holländer, T. Stoica, G. Mussler, U. Breuer, J. M. Hartmann, D. Grützmacher, and S. Mantl, "SiGeSn growth studies using reduced pressure chemical vapor deposition towards optoelectronic applications," Thin Solid Films **557**, 183–187 (2014).

12. T. Yamaha, O. Nakatsuka, S. Takeuchi, W. Takeuchi, N. Taoka, K. Araki, K. Izunome, and S. Zaima, "Growth and characterization of heteroepitaxial layers of GeSiSn ternary alloy," ECS Trans. **50**(9), 907–913 (2013).
13. R. T. Beeler, D. J. Smith, J. Kouvetakis, and J. Menéndez, "GeSiSn photodiodes with 1 eV optical gaps grown on Si(100) and Ge(100) platforms," IEEE J. Photovoltaics **2**(4), 434–440 (2012).
14. P. Moontragoon, R. A. Soref, and Z. Ikonic, "The direct and indirect bandgaps of unstrained $Si_xGe_{1-x-y}Sn_y$ and their photonic device applications," J. Appl. Phys. **112**(7), 073106 (2012).
15. G. Sun, R. A. Soref, and H. H. Cheng, "Design of a Si-based lattice-matched room-temperature GeSn/GeSiSn multi-quantum-well mid-infrared laser diode," Opt. Express **18**(19), 19957–19965 (2010).
16. R. Soref, "Silicon-based silicon-germanium-tin heterostructure photonics," Philos. Trans. R. Soc., A **372**(2012), 20130113 (2014).
17. D. B. Williams and C. B. Carter, *Transmission Electron Microscopy: A Textbook for Materials Science* (Springer, 2009).
18. N. Taoka, T. Asano, T. Yamaha, T. Terashima, O. Nakatsuka, I. Costina, P. Zaumseil, G. Capellini, S. Zaima, and T. Schroeder, "Non-uniform depth distributions of Sn concentration induced by Sn migration and desorption during GeSnSi layer formation," Appl. Phys. Lett. **106**(6), 061107 (2015).
19. O. Madelung, ed., *Semiconductors: Group IV Elements and III–V Compounds.* (Springer, 1982).
20. V. R. D'Costa, C. S. Cook, J. Menéndez, J. Tolle, J. Kouvetakis, and S. Zollner, "Transferability of optical bowing parameters between binary and ternary group-IV alloys," Solid State Commun. **138**(6), 309–313 (2006).
21. S. Sant and A. Schenk, "Pseudopotential calculations of strained-GeSn/SiGeSn hetero-structures," Appl. Phys. Lett. **105**(16), 162101 (2014).
22. M. Jaros, "Simple analytic model for heterojunction band offsets," Phys. Rev. B Condens. Matter **37**(12), 7112–7114 (1988).
23. C. G. Van de Walle, "Band lineups and deformation potentials in the model-solid theory," Phys. Rev. B Condens. Matter **39**(3), 1871–1883 (1989).
24. P. Harrison, *Quantum Wells, Wires, and Dots: Theoretical and Computational Physics of Semiconductor Nanostructures* (John Wiley & Sons, 2005).
25. L. M. Giovane, H.-C. Luan, A. M. Agarwal, and L. C. Kimerling, "Correlation between leakage current density and threading dislocation density in SiGe p-i-n diodes grown on relaxed graded buffer layers," Appl. Phys. Lett. **78**(4), 541 (2001).
26. M. Oehme, K. Kostecki, M. Schmid, M. Kaschel, M. Gollhofer, K. Ye, D. Widmann, R. Koerner, S. Bechler, E. Kasper, and J. Schulze, "Franz-Keldysh effect in GeSn pin photodetectors," Appl. Phys. Lett. **104**(16), 161115 (2014).

1. Introduction

Recent years have seen a lot of experimental effort directed towards integrating photonics with electronics. The Group-IV elements Si and Ge are the dominating materials of semiconductor electronics. However, their application to optoelectronics is limited due to their indirect bandgap and the concomitant low efficiency in optoelectronic applications. Recent experiments have, therefore, focused on the investigation of GeSn and SiGeSn alloys that could potentially be used as direct bandgap Group-IV-materials for an efficient on-chip integration of photonics and electronics. The relaxed alloy $Ge_{1-y}Sn_y$ has been predicted to become a direct bandgap material for y > 0.073 [1], while pseudomorphic $Ge_{1-y}Sn_y$ is predicted to have a direct bandgap for y > 0.19 [2]. A number of experimental studies have been performed to fabricate and characterize $Ge_{1-y}Sn_y$ bulk [3–6] and quantum well [7] photodetector devices. Because of the large lattice mismatch between Ge and Sn (14%), the growth of $Ge_{1-y}Sn_y$ alloys with a large percentage of Sn is difficult to achieve on Si and Ge substrates. The ternary alloy SiGeSn allows one to decouple bandgap and lattice constant [8] and is, therefore, a particularly interesting candidate for optoelectronic applications. Several groups have reported the successful fabrication of SiGeSn alloys by Chemical Vapor Deposition (CVD) [9–11] and Molecular Beam Epitaxy (MBE) [12]; bulk SiGeSn-photodiodes have been fabricated and analyzed [13]. Furthermore, a number of proposals concerning photonic devices such as light-emitting diodes or modulators with Multi-Quantum-Well (MQW) structures in their active regions have been made [14, 15]. For those devices additional advantages such as a lower intensity of Auger processes have been predicted [16].

Many suggested devices rely on the existence of high quality GeSn buffer layers with a high concentration of Sn, proposing $Ge_{1-y}Sn_y$ quantum wells with a direct bandgap in the active layer of the devices. Here, we report on the fabrication and characterization of SiGeSn

MQW photodiodes on Ge in order to make use of existing, well-developed Ge virtual substrate (VS) technology. We present results on the diode characteristics, optical responsivity and electroluminescence and extract the value of the bandgap of the well regions from the absorption coefficient. Finally, we compare our result with theoretical predictions from band structure calculations.

2. Layer growth and characterization

The SiGeSn MQWs are deposited by means of solid-source MBE on 4" substrates. Si is deposited by means of an electron beam evaporator, whereas both Ge and Sn are evaporated from effusion cells. Dopant sources are B (p-type) and Sb (n-type). Fluxes of the Sn and Ge effusion cells, as well as of the Si electron beam evaporator, were calibrated separately and adjusted to obtain a total growth rate of 1 Å/s. The MBE layer stacks are shown schematically in Fig. 1(a). Layer growth started with 400 nm of B-doped Si ($N_A = 1 \times 10^{20}$ cm^{-3}). A 50 nm layer of B-doped Ge ($N_A = 1 \times 10^{20}$ cm^{-3}) was then deposited at a growth temperature of $T_S =$ 330 °C and annealed at 810 °C in order to obtain a high quality, plastically relaxed Ge epi-layer, serving as a VS for subsequent epitaxial growth. Layer deposition continued with another 50 nm of B-doped Ge ($N_A = 1 \times 10^{20}$ cm^{-3}), and 10 nm of undoped Ge, followed by a second annealing step. Prior to the deposition of the undoped SiGeSn barrier and well layers, the growth was interrupted to lower the growth temperature down to 160 °C. Two samples, one with a 2-QW structure and one with a 4-QW structure, were fabricated, in which the barrier layers and the quantum well layers have a thickness of 10 nm, each. The barrier and well layers are composed of SiGeSn with different fractions of the constituent semiconductor materials. The material compositions were chosen not only for their bandgaps but also such that the lattice constant of the unstrained well (barrier) material is larger (smaller) than that of Ge with the aim of obtaining only small residual strain of the total MQW layer stack on the Ge VS. A 10 nm-thick undoped Ge layer was then deposited as a spacer to separate the heterojunction from the doping transition. After the growth of 100 nm of Sb-doped Ge ($N_D \approx 5 \times 10^{19}$ cm^{-3}), the growth temperature was increased to 400 °C, and 100 nm of Sb-doped Si ($N_D \approx 5 \times 10^{19}$ cm^{-3}) were deposited as the final layer.
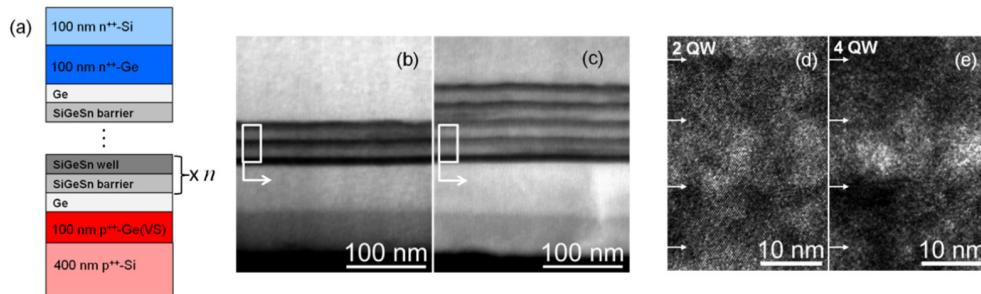

Fig. 1. (a) Schematic cross section of the MBE layer stacks. (b) and (c) HAADF-STEM image of the MBE layer stacks of the 2-QW and 4-QW sample, respectively. The image contrast represents the atomic number (Z), where black corresponds to low and white to high Z, respectively. (d) and (e) HR-TEM images of the MBE layer stacks of the 2-QW and 4-QW sample, respectively, corresponding to the areas highlighted in the HAADF-STEM images.
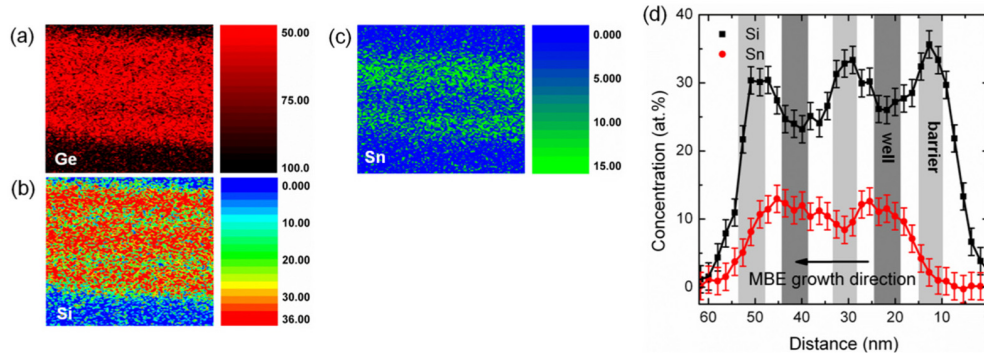
Fig. 2. (a)-(c) EDS maps of the well and barrier regions of the 2-QW sample with concentrations in at.%. (d) EDS line scan of the well and barrier regions of the 2-QW sample. Light grey bars indicate the data points that were selected to extract the barrier composition, dark gray bars indicate the data points that were selected to extract the well composition.

We investigated the MBE layers using Transmission Electron Microscopy (TEM) as shown in Figs. 1(b)–1(e), using a JEOL JEM–2010F microscope. Figures 1(b) and 1(c) show High-Angle Annular Dark Field Scanning TEM (HAADF-STEM) images of the MBE layer stacks of the 2-QW and 4-QW device. The image contrast is strongly related to the atomic number (Z), so that black corresponds to lighter regions than white [17]. A clear difference in composition can be seen between the well and barrier layers. Figures 1(d) and 1(e) show HR-TEM images of the MBE layer stacks with clearly resolved crystallinity of well and barrier layers. The periodicity of 20 nm for well and barrier layers is confirmed and barrier as well as well layers are of approximately equal thickness.

We investigated the material compositions of well and barrier by means of Energy Dispersive Spectroscopy (EDS) as well as by X-Ray Diffraction (XRD). For the EDS analysis a probe beam with a diameter of 0.7 nm was used to extract the position-dependent composition from the sample cross section with a spatial resolution of about 2 nm and an estimated accuracy of ± 2.0%. This accuracy was previously determined for the system with a known standard. The presence of Si-rich barrier and Sn-rich well regions can be observed qualitatively in the 2D maps of Si, Ge and Sn content shown in Figs. 2(a)-2(c), respectively. We quantitatively extract the Si, Sn and Ge content in barriers and wells from the EDS linescan shown in Fig. 2(d) by selecting those data points that can be attributed to barrier or well regions. The resulting values are shown in Table 1. We note that the Sn content of the middle barrier layer does not seem to drop significantly from its value in the well layers. A possible explanation is that although growth temperatures were kept low, some Sn diffusion could have smeared out the transition region between barrier and well layers [18].

Table 1. Composition of barrier and well layers in at%.

	Si	Ge	Sn
Barrier	31.2 ± 4.4	62.3 ± 5.3	6.5 ± 4.0
Well	25.2 ± 2.1	63.4 ± 2.3	11.4 ± 2.5

XRD analysis with PANalytical Empyrean was used to characterize both samples. Reciprocal space maps (RSM) taken along the (224) direction in combination with ω-2θ-scans along the (004) direction are shown in Figs. 3(a) and 3(b) for the two samples.
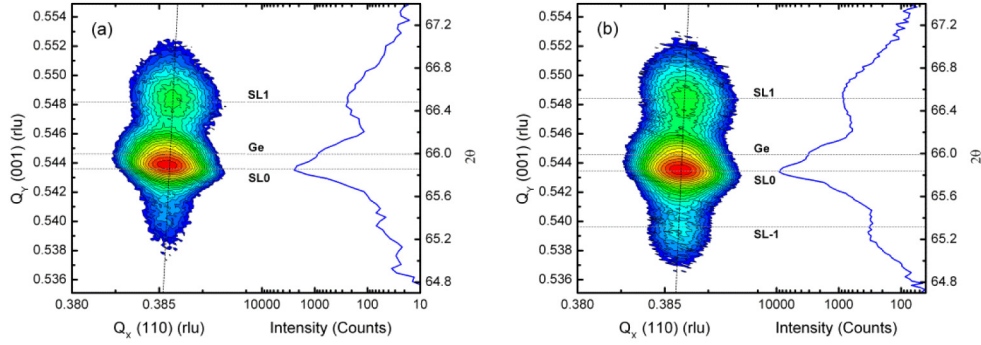
Fig. 3. Reciprocal space maps taken along the (224) direction and ω-2θ-scans taken along the (004) direction for (a) the 2-QW sample and (b) the 4-QW sample.

Both ω-2θ-scans show a double peak structure at 2θ ~66° that can be attributed to a superposition of the Ge buffer with the zero-order superlattice peak (SL0). The fact that both the Ge peak and the SL0 peak can be resolved indicates that the MQW layers are not perfectly lattice matched with the Ge. In addition, one (2-QW sample) or two (4-QW sample) satellite peaks are observed on each side of the SL0 peak (SL1, SL-1). Further peaks originating from the MQW structures cannot be resolved as a consequence of the small number of periods. We used information on the in-plane as well as out-of plane lattice constants from both the ω-2θ-scan and the RSM to identify the Ge peak based on the unstrained Ge lattice constant, $a_{0,Ge}$ = 0.5657. The position of the Ge peak yields a lattice parameter along the growth direction of $a_{Ge}^{\perp}$ = 0.5662 nm and 0.5663 nm for the 2-QW and 4-QW samples, respectively, indicating that approximately 0.1% of compressive strain is present in the Ge in both samples as a result of the growth on Si. The measured average off-plane lattice parameters $a_{MQW,m}^{\perp}$ for the SiGeSn well and barrier layers, are shown in Table 2 for both the 2-QW and 4-QW samples. The MQW periodicity can be obtained from the distance of the superlattice peaks to the SL0 peak as 17.8 ± 2.3 nm, in agreement with TEM results.

Table 2. MQW lattice constants determined by experiment and predicted based on EDS composition analysis

	2-QW	4-QW
$a_{MQW,m}^{\perp}$ (ω-2θ-scan)	0.5673 nm	0.5674 nm
$a_{MQW,m}^{\parallel}$ (RSM)	0.5655 nm	0.5650 nm
$a_{MQW,c}^{\perp}$ (calculated)	(0.5677 ± 0.0058) nm	(0.5681 ± 0.0058) nm

The RSM gives qualitative and quantitative information on the strain state of the MQW layers. For both samples it can clearly be observed that the MQW layers are not fully pseudomorphic, as indicated by the slightly tilted alignment of the MQW peaks. The average in-plane lattice constant $a_{MQW,m}^{\parallel}$ of barrier and well layers as extracted from the position of the SL0 peak in the RSM is shown in Table 2. It allows us to compare XRD results with calculation based on the composition obtained from EDS analysis using

$$a_i^{\perp} = -2\frac{C_{12}^i}{C_{11}^i}(a_{MQW,m}^{\parallel} - a_{0,i}) + a_{0,i}, \tag{1}$$

where i stands for barrier or well. The elastic constants C_{11}^i and C_{12}^i as well as the lattice constant of the relaxed SiGeSn barrier or well layer $a_{0,i}$ are obtained by linear interpolation between the corresponding values for the constituent materials Si, Ge and Sn, obtained from

Ref [19]. The average lattice constant $a^{\perp}_{MQW,c} = (a^{\perp}_{barrier} + a^{\perp}_{well})/2$ of the SiGeSn layers obtained from this calculation is shown in Table 2 and compares well to the value obtained from the ω-2θ-scan.

Table 3. Bowing parameters of the binary alloys

	$b^{SiGe}_{g,\zeta}$	$b^{GeSn}_{g,\zeta}$	$b^{SiSn}_{g,\zeta}$
Γ [eV]	0.21[a]	2.46[b]	13.2[c]
L [eV]	0.335[a]	0.99[b]	2.124[a]

[a]From J. Appl. Phys. **112**, 073106 (2012), [b]from arXiv preprint arXiv:1406.0448 (2014). [c]From PRL **102**, 107403 (2009).

We, thus, take the values of Si, Ge, and Sn as obtained from EDS analysis as a basis for an effective mass band structure calculation to predict the optoelectronic properties of the MQW structures. In this calculation the model parameters for the $Si_xGe_{1-x-y}Sn_y$ barrier and well are obtained using a linear interpolation of the model parameters for Si, Ge, and α-Sn, except for the bandgaps and effective masses. For the bandgaps the following quadratic interpolation has been used [20]:

$$E_{g,\zeta}(Si_xGe_{1-x-y}Sn_y) = x \cdot E_{g,\zeta}(Si) + (1-x-y) \cdot E_{g,\zeta}(Ge) + y \cdot E_{g,\zeta}(Sn)$$
$$- b^{SiGe}_{g,\zeta} \cdot x \cdot (1-x-y) - b^{GeSn}_{g,\zeta} \cdot y \cdot (1-x-y) - b^{SiSn}_{g,\zeta} \cdot x \cdot y. \tag{2}$$

Here, $b^{SiGe}_{g,\zeta}$, $b^{GeSn}_{g,\zeta}$, and $b^{SiSn}_{g,\zeta}$ are the bowing parameters and $\zeta = \Gamma, L$ refers to the different conduction valleys. The bowing parameters that were used in the calculation are listed in Table 3. For the effective mass an interpolation according to [21] has been used. Band offsets between materials are approximated according to Jaros [22]. We used model-solid theory to estimate the effects of strain on the band structure [23]. The effects of confinement are calculated using effective mass theory [24]. Due to considerable uncertainties of the material parameters, particularly the bowing parameters, we limit our calculation to an idealized 10 nm single quantum well. The resulting potential profile of the MQW layers for
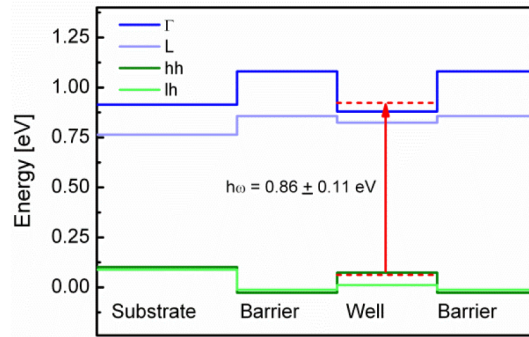

Fig. 4. Theoretical calculation of the potential profile of the MQW layers for $Si_{0.252}Ge_{0.634}Sn_{0.114}$ wells and $Si_{0.312}Ge_{0.623}Sn_{0.065}$ barriers with a substrate lattice constant of 0.5650 nm.
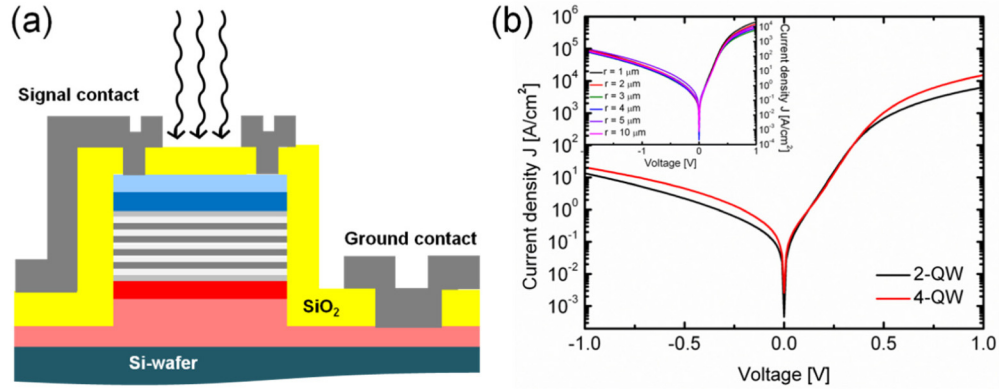
Fig. 5. (a) Schematic cross section (b) Current density as a function of voltage for a 2-QW (black) and the 4-QW (red) device with device radii of 5 μm. The inset shows the current density-voltage characteristics of the 2-QW devices for devices with different radii. The current scales with device area.

$Si_{0.252}Ge_{0.634}Sn_{0.114}$ wells and $Si_{0.312}Ge_{0.623}Sn_{0.065}$ barriers, and with a substrate lattice constant of 0.5650 nm, is shown in Fig. 4. Our theoretical model predicts the well regions to be indirect-bandgap alloys and the barriers to provide type-I alignment. Taking into account uncertainties in the experimental determination of composition (Table 1) as well as confinement, the transition energy is calculated to be 0.86 ± 0.11 eV.

3. Device fabrication and characterization

The photodiodes were fabricated using a lithographic process leading to single mesa structures. A schematic cutaway-image of the device is shown in Fig. 5(a). An inductively coupled plasma reactive ion etching process (ICP-RIE) based on Cl_2/HBr was used to define the mesa-structure. A 300 nm thick SiO_2 layer was then used to passivate the mesa. After structuring the contact holes, 800 nm of Al (as CMOS-compatible contact metal) were deposited and structured to form signal and ground contacts.
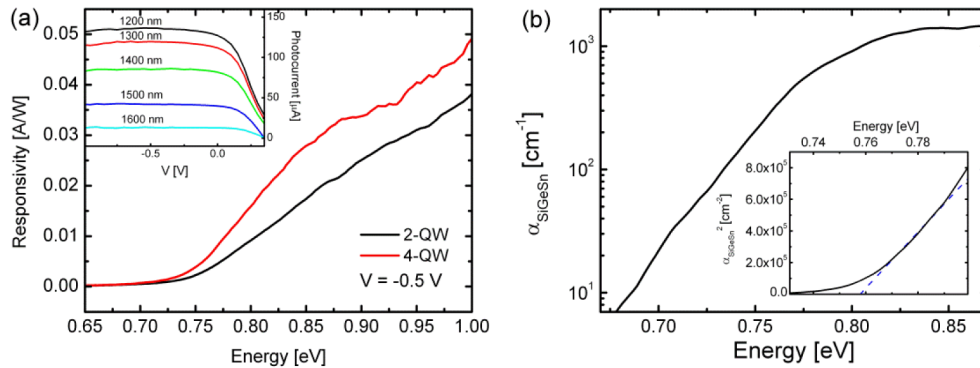

Fig. 6. (a) Responsivity of a 2-QW device and a 4-QW device at −0.5 V external bias. The responsivity is enhanced for the 4-QW device. The inset shows photocurrents of a 2-QW device under reverse bias and at different wavelengths. (b) Absorption coefficient of the SiGeSn-well regions as a function of incident photon energy and at zero bias. The inset shows the square of the absorption coefficient as a function of photon energy and a linear fit to the data. From the intersection of the fit line with the energy axis we obtain a bandgap energy of ~0.76 eV.

All samples were characterized electrically with a Keithley 4200 semiconductor analyzer. Optical responsivities were measured with a super continuum light source equipped with an

acousto-optical tunable filter in order to achieve narrow output spectra over a broad wavelength range. A single mode fiber probe was used to couple light into the detector in vertical incidence. An extended InGaAs-detector was used to measure laser output power. Photocurrents and dark currents were measured with an on-wafer semiconductor analyzer.

Figure 5(b) shows the current density-voltage characteristics for a 2-QW and 4-QW diode with device radii of 5 μm, each. For both samples, the dark currents are comparable. Since dark currents are directly influenced by the number of threading dislocations [25], this indicates that defect-related nonradiative recombination processes should also have comparable influence on photocurrent measurements of both diodes.

As shown in the inset of Fig. 6(a), the photocurrents are constant under reverse bias for all wavelengths investigated. As a result, we can assume that the number of electrons generated per photon does not depend on the bias, i.e. there is no avalanching. As the intrinsic zone of the PIN-photodiodes consists of SiGeSn layers sandwiched between two Ge layers with a thickness of 10 nm each, we can expect photocurrents to be generated in the Ge layers as well as in the SiGeSn quantum wells. Figure 6(a) shows the optical responsivity R_{opt} (photocurrent per unit optical power) as a function of photon energy E_{ph} (0.65 eV ≤ E_{ph} ≤ 1.0 eV) at room temperature obtained from PIN-photodiodes with a radius of 5 μm each. The optical responsivity is clearly enhanced in the 4-QW device compared to the 2-QW device as a result of the contribution from the additional two quantum wells. At an incident photon energy of 0.9 eV we obtain R_{opt} = 0.033 for the 4-QW device and R_{opt} = 0.025 for the 2-QW device, which is considerably smaller than e.g. R_{opt} = 0.21 measured for a bulk Ge PIN-photodiode with a 300 nm intrinsic zone at the same energy [26]. This difference is mainly due to the small thickness of the active layers in our devices. The internal quantum efficiency η_{int} of the devices is the ratio of the number of photoelectrons produced for every photon incident on the photosensitive surface and is obtained as follows:

$$\eta_{int} = R_{opt} \cdot (1-R)^{-1} \cdot \frac{h \cdot c}{q \cdot \lambda} \qquad (3)$$

where R is the surface reflection, which was measured for both samples, λ is the wavelength and q, c and h are the electron charge, the speed of light, and the Planck constant, respectively. For a fully depleted PIN-photodiode with negligible penetration of the electric field into the doping layers, we can use Beer's law to derive the following expression for the internal quantum efficiency η_n of a device with n wells:

$$\eta_n = \exp(-\alpha_{Ge} \cdot d_{n,Ge}) \cdot (1 - \exp(-2 \cdot \alpha_{Ge} \cdot d_S - n \cdot \alpha_W \cdot d_W - (n+1) \cdot \alpha_B \cdot d_B)) \qquad (4)$$

Here, α_{Ge} is the absorption coefficient of Ge, $d_{n,Ge}$ is the thickness of the Ge part of the n-doped heterojunction top contact, d_s is the thickness of the Ge spacer layers in the intrinsic zone of the device, α_W denotes the absorption coefficient and d_W the thickness of a well region. Neglecting the contribution of the barrier regions to the internal quantum efficiency for photon energies below the barrier bandgap energy, and combining the data from both devices allows us to eliminate the contributions from the Ge spacer layers. We determine the absorption coefficient of the well regions as follows:

$$\frac{1 - \eta_4 \cdot \exp(\alpha_{Ge} \cdot d_{n,Ge})}{1 - \eta_2 \cdot \exp(\alpha_{Ge} \cdot d_{n,Ge})} = \exp(-2 \cdot \alpha_W \cdot d_W) \qquad (5)$$

We assume that the absorption coefficients of the well regions of the 2-QW-sample and 4-QW-sample are identical. In particular, we neglect the fact that the internal electric fields at zero bias in the intrinsic zones of the 2-QW-sample and the 4-QW-sample differ due to the difference in thickness (70 nm for the 2-QW-sample, 110 nm for the 4-QW-sample). This difference in electric field leads to a slightly different modification of the absorption edge

(Franz-Keldysh effect) for the two samples but it does not shift the bandgap energy. Data for the absorption coefficient of Ge are taken from [26]. The absorption coefficient is plotted as a function of photon energy in Fig. 6(b). We do not observe any clear indications of type-I confinement, which could be a consequence of the small number of quantum well regions or of weak confinement for holes in the valence band, see Fig. 4. For the purpose of extracting the bandgap energy we, therefore, consider the SiGeSn well regions as bulk material, for which $\alpha^2 \sim (E - E_{g,W})$. Here, we also assume that although the SiGeSn well regions are indirect-bandgap alloys, the photocurrent originates from the direct transition since the difference in energy between the direct and the indirect bandgap is predicted to be small (see Fig. 4). From the fit, we obtain $E_{g,W} \sim 0.76$ (see inset of Fig. 6(b)).

In Fig. 7 we show the room-temperature electroluminescence (EL) measurements at different injection current performed on PIN-photodiodes with a radius of 80 μm. Again, we can expect contributions from the SiGeSn well regions and from the Ge spacer layers. The EL intensity of the 4-QW-sample is lower than that of the 2-QW-sample, which can be a result of a higher defect density in that particular device. Nonetheless, we observe that the 4-QW-sample shows an increase in EL intensity towards lower energies compared to 2-QW-sample as a result of $E_{g,W} < E_{Ge}$, which is consistent with the observation from absorption data. The shift of the peak to lower energies as the injection current is increased, is a consequence of the increase in device temperature and the resulting decrease in bandgap energy.
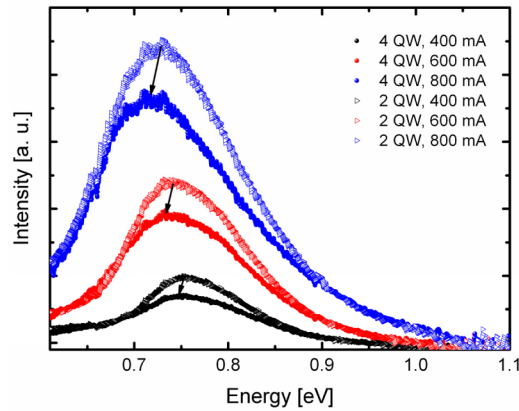

Fig. 7. Room-temperature electroluminescence measurements of the 2-QW and 4-QW device with diode radii of 80 μm each.

We can expect the photocurrent as well as the room-temperature EL to originate from direct transitions within the wells. We find that $E_{g,W}$ extracted from experiment (0.76 eV) is within the range predicted by bandstructure calculations (0.86 ± 0.11 eV). Nonetheless, we point out that the inaccuracy of the parameters available for the theoretical calculations could be significant. In particular, the bowing parameter $b_{g,\Gamma}^{SiSn}$ has a large influence on the results of the bandgap predictions. There are experimental indications that this parameter is not constant over the entire composition range of the binary alloy $Si_{1-y}Sn_y$. While setting $b_{g,\Gamma}^{SiSn}$ to 13.2 eV seems to be appropriate for y ~0.2, a value of $b_{g,\Gamma}^{SiSn} \sim 4$ eV has also been reported for y ~0.5 [8]. At the moment, there is insufficient experimental data to reliably predict the bandgap energies for all $Si_xGe_{1-x-y}Sn_y$ alloy compositions.

4. Conclusion

We demonstrate the successful fabrication and characterization of SiGeSn-MQW-photodiodes. We observe a clear contribution of the SiGeSn well regions to both optical

responsivity and room-temperature EL spectra. Furthermore, the predictions made by our idealized theoretical model are consistent with experimental results. We thus find that even highly strained SiGeSn-MQW-layers can be grown on VS with a defect density that is sufficiently low to permit opto-electronic device operation.

MQW-photodiodes with barrier and well regions composed of $Si_xGe_{1-x-y}Sn_y$ are extremely interesting because they can be designed to be strain-relaxed on VS. In this way, the well-developed VS technology can be used for possible complementary metal-oxide-semiconductor (CMOS) integration. Moreover, by adjusting the alloy compositions and, thus, the bandgaps of the wells, the devices can be tuned over a broad range of wavelengths. More data is needed, in particular to determine the bowing parameters of SiSn alloys over a broad range of compositions. This could further improve the agreement between theory and our experimental results and will allow one to determine whether SiGeSn-MQW-photodiodes can be designed to be strain-relaxed on Ge with a direct bandgap well material and type-I alignment provided by the barriers.

Acknowledgments